

# Journal Pre-proof

The Cardiff Eye Shape Analysis Protocol (CESAP): producing a digital representation of the anterior ocular surface

Jennifer M. Turner, Chi Hieu Le, Paul J. Murphy



PII: S2405-8440(25)00981-8

DOI: <https://doi.org/10.1016/j.heliyon.2025.e42601>

Reference: HLY 42601

To appear in: *HELIYON*

Received Date: 17 July 2024

Revised Date: 31 January 2025

Accepted Date: 10 February 2025

Please cite this article as: J.M Turner, C.H. Le, P.J Murphy, The Cardiff Eye Shape Analysis Protocol (CESAP): producing a digital representation of the anterior ocular surface, *HELIYON*, <https://doi.org/10.1016/j.heliyon.2025.e42601>.

This is a PDF file of an article that has undergone enhancements after acceptance, such as the addition of a cover page and metadata, and formatting for readability, but it is not yet the definitive version of record. This version will undergo additional copyediting, typesetting and review before it is published in its final form, but we are providing this version to give early visibility of the article. Please note that, during the production process, errors may be discovered which could affect the content, and all legal disclaimers that apply to the journal pertain.

© 2025 Published by Elsevier Ltd.

1 **The Cardiff Eye Shape Analysis Protocol (CESAP): producing a digital representation of**  
2 **the anterior ocular surface**

3  
4 Jennifer M Turner<sup>a</sup>, Chi Hieu Le<sup>b</sup> and Paul J Murphy<sup>c</sup>

5  
6 <sup>a</sup>Cardiff University, School of Optometry and Vision Sciences, Maindy Road, Cardiff, CF24 4HQ, UK

7 <sup>b</sup>University of Greenwich, School of Engineering, Central Avenue, Medway, ME4 4TB, UK

8 <sup>c</sup>University of Waterloo, School of Optometry and Vision Science, University Avenue West, Waterloo, N2L 3G1,  
9 Canada

10  
11 Tables: 2, Figures: 10

12  
13 Address for correspondence:

14 Prof Paul J Murphy

15 University of Waterloo

16 School of Optometry and Vision Science

17 200 University Avenue West

18 Waterloo, N2L 3G1

19 Ontario, Canada

20  
21 Email: [pjmurphy@uwaterloo.ca](mailto:pjmurphy@uwaterloo.ca)

22  
23 Funding: This study was supported by a collaborative partnership between Cardiff University and Menicon  
24 (Japan) Ltd. The authors have no proprietary or commercial interests in any of the materials discussed in this  
25 article.

26

27

28 **ABSTRACT**

29

30 **Objective:** To develop a method for accurate 3-dimensional (3D) representation of the anterior ocular surface  
31 (AOS) based on ocular impression and reverse engineering of an AOS plaster biomodel.

32 **Methods:**

33 An AOS plaster biomodel was fabricated using ocular impression and a developed casting support device (CSD)  
34 and landmark registration element (LRE) to stabilise and consistently fix the impression casting tray within the  
35 casting support during the casting process. The touch-trigger probe on a co-ordinate measurement machine  
36 (CMM) digitized the AOS plaster biomodel to represent the AOS shape. The CSD and LRE were manufactured  
37 using an Additive Manufacturing selective laser sintering (SLS) process. A single stainless-steel ball (diameter: 22  
38 mm) was cast as a surrogate AOS biomodel using polyvinylsiloxane impression material. The surrogate biomodel  
39 which was used to evaluate material selection and stability of the AOS biomodels fabricated using the CSD and  
40 LRE, and to evaluate repeatability and reproducibility of the point cloud data collection methods. The points of  
41 circular profiles were measured at different Z values in mm:  $z = -1$  mm,  $z = -2$  mm,  $z = -3$  mm,  $z = -4$  mm and  $z$   
42  $= -5$  mm.

43 **Results:** The measurements were highly repeatable with an acceptable tolerance. For the typical case of the  
44 surrogate AOS biomodel, the average distance of the digitised points to the best-fit sphere of all the digitised points  
45 from four measurements ranges from 0.002 to 0.010 mm. The shrinkage study of the surrogate AOS biomodels  
46 was conducted, with measurements taken one month apart for comparison. The analysis results showed that most  
47 of the surrogate AOS biomodels reduced in size but within an acceptable tolerance, in which the mean error is  
48 from 0.005 to 0.010 mm for the 2D circular profiles measured at  $Z = -4$  mm.

49 **Conclusions:** The Cardiff Eye Shape Analysis Protocol (CESAP) provides a repeatable and consistent method for  
50 producing solid, white-plaster, representations of a plaster cast AOS biomodel. Casting an impression in white  
51 plaster (Novadur™) produces a consistent surrogate AOS biomodel of a single stainless-steel 22 mm diameter  
52 ball. CESAP can be used as a framework for consistently converting an ocular impression into a 'real' AOS model that  
53 can be reverse-engineered to create 3D CAD models of the AOS shape for potential applications in optical image  
54 (topographer) calibration, prosthetic shell and scleral lens design, and AOS database development.

55 **Keywords:** corneal topography, ocular surface shape, impression moulding, laser scanning, scleral lens

56 **Highlights:**

- 57 • The Cardiff Eye Shape Analysis Protocol (CESAP) provides a repeatable and consistent method for producing  
58 solid white plaster representations of a model anterior ocular surface (AOS).
- 59 • White plaster (Novadur™) produces a consistent representation of a model (AOS).

## 60 1. INTRODUCTION

61 Knowledge of anterior ocular surface (AOS) topography is important for contact lens fitting, ocular disease  
62 diagnosis, and ocular surgery planning. In particular, the shape and smoothness of the corneal surface forms a  
63 key component in the ocular optical system to produce a clear image on the retina. The measurement of AOS  
64 topography can be performed using optical reflectometry methods to produce a virtual topographical map [1],  
65 but an actual plaster cast model can also be produced using the impression moulding method [2]. Ocular  
66 impressions are used in the manufacture of custom scleral contact lenses and ocular prostheses [2-4]. An  
67 impression is taken of the eye using a plastic material that can be manipulated to mould to the shape of the eye,  
68 before rapidly setting as a negative image of the ocular surface shape [5]. From this mould, a positive plaster-  
69 cast is taken, which is used to guide scleral lens manufacture [6].

70

71 With the increasing use of scleral lenses for treating ocular surface disease, there is a renewed interest in  
72 understanding how the AOS changes across the limbal transition zone between the cornea and the sclera [6-10],  
73 Although wide-field optical topographers that can image the limbal zone are available [7, 11-13], an actual  
74 representation of the AOS is of value in determining the reliability of these corneal topographers by comparing  
75 the virtual topographical map with the actual model determined using impression moulding. This has led to a  
76 return of interest in impression moulding [4].

77

78 Anatomical registration is an important requirement of the impression-making process since it is critical that  
79 both the mould and cast model are 'registered' correctly with the ocular anatomy. The clinical impression  
80 method described by Pullum (and summarised above) is sufficient for general clinical purposes [2], but it lacks  
81 reliability when undertaking ocular impression where the accurate measurement of anatomical features,  
82 registered according to the three cardinal meridians ( $x, y, z$ ), is required, such as when assessing AOS topographer  
83 accuracy [10]. To our knowledge, there is no published report on a method to optimise anatomical registration  
84 when using ocular impression moulding.

85

86 This study therefore had two objectives: to develop a reliable method for anatomical registration of the AOS  
87 with the impression mould and the resultant plaster cast; and to assess whether the developed registration method  
88 was reliable in producing a precise and repeatable biomodel of the AOS shape (repeatability and reproducibility  
89 (R&R) study).

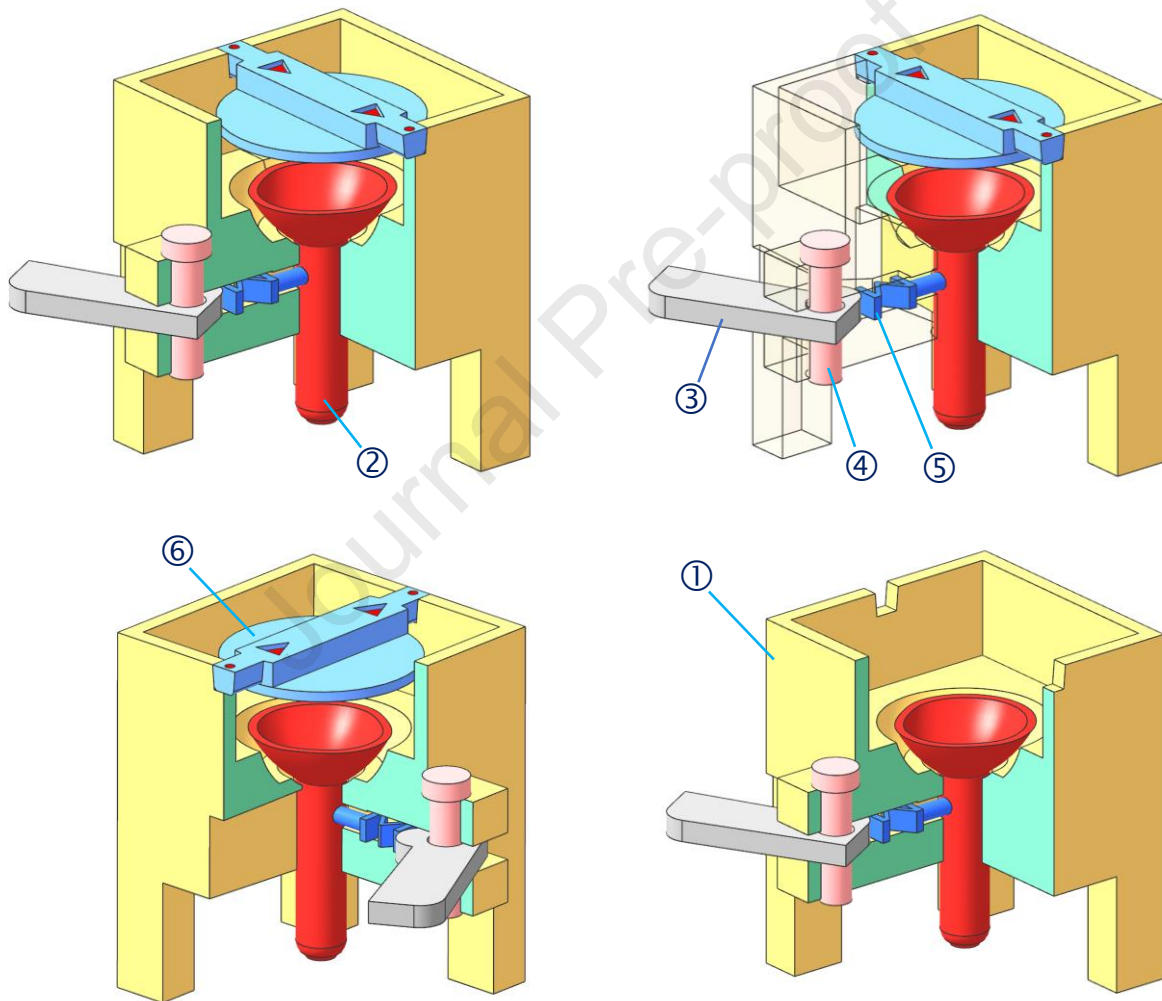
90

## 91 2. METHODS

### 92 *Casting support and landmark registration element design*

93 In order to reconstruct a three-dimensional (3D) model of the eye shape from the ocular impression casting trays

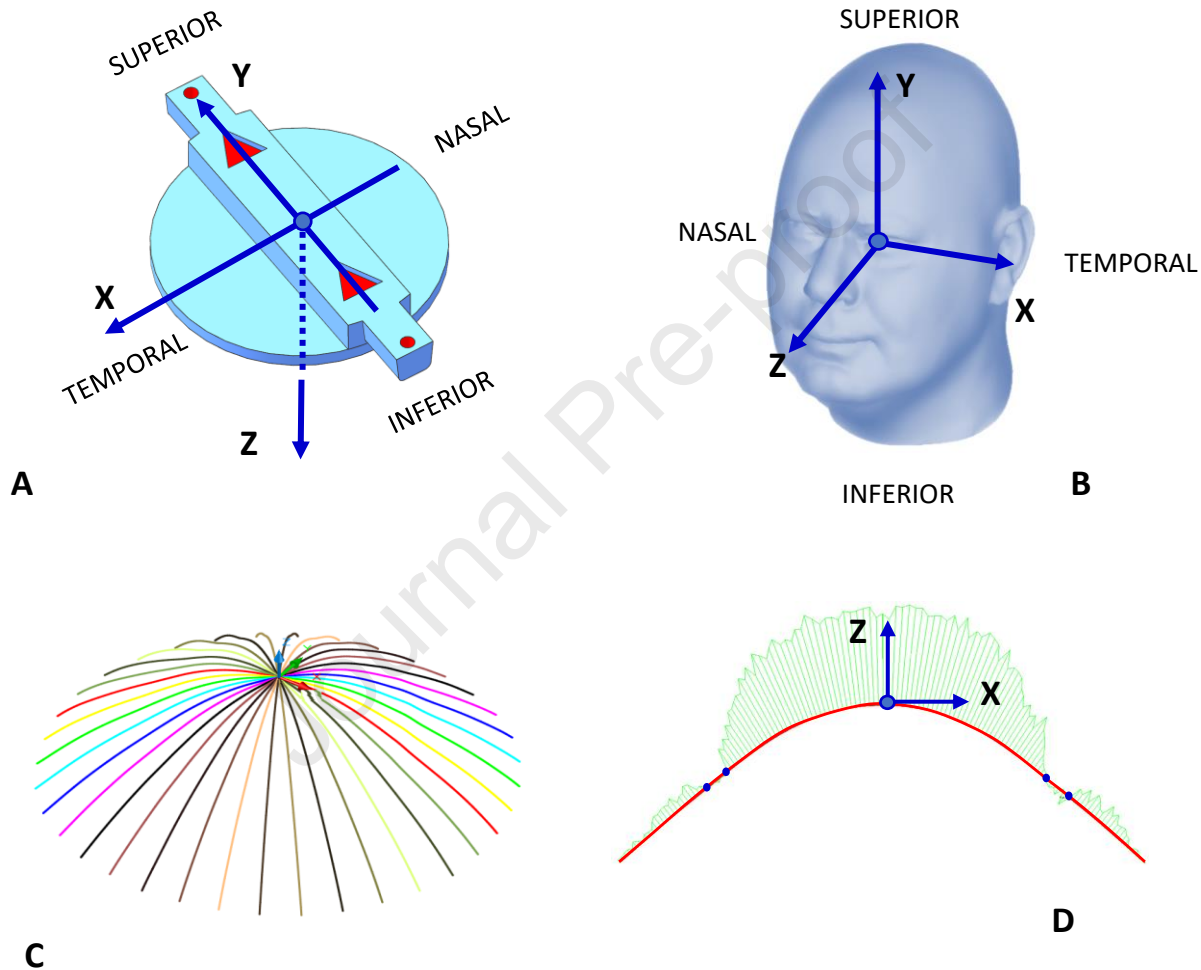
94 (Cantor and Nissel Ltd, Brackley, UK), a casting support device and a registration element were designed and  
 95 manufactured. Figure 1 presents the 3D CAD (Computer Aided Design) assembly models of a casting support  
 96 device and a registration element. The important design objective is that the impression casting tray needs to  
 97 be stably and consistently fixed to the casting support during the casting process of fabricating the AOS plaster  
 98 cast biomodel of the eye shape. In addition, to support a systematic investigation of a big number of 3D eye  
 99 shapes, the ocular impression casting trays need to be correctly aligned with the relevantly used datum for  
 100 processing 3D scanned point cloud data. With the design shown in Figure 1, a locking mechanism with a spring  
 101 element was introduced to fix an impression casting tray to the main frame of a device.



123 Figure 1: 3D CAD assembly models with section views of a casting support device in assembly with a landmark  
 124 registration element (LRE) including the following: A main frame (1), an impression casting tray (2), a locking  
 125 mechanism (3-5) in which a spring (5) is introduced to fix an impression casting tray (2) to a main frame (1), and  
 126 a landmark registration element (6) which is aligned with an impression tray (2) and a main frame (1).  
 127

128 To maintain the correct alignment of the impression casting tray within the vertical eye meridian, a landmark

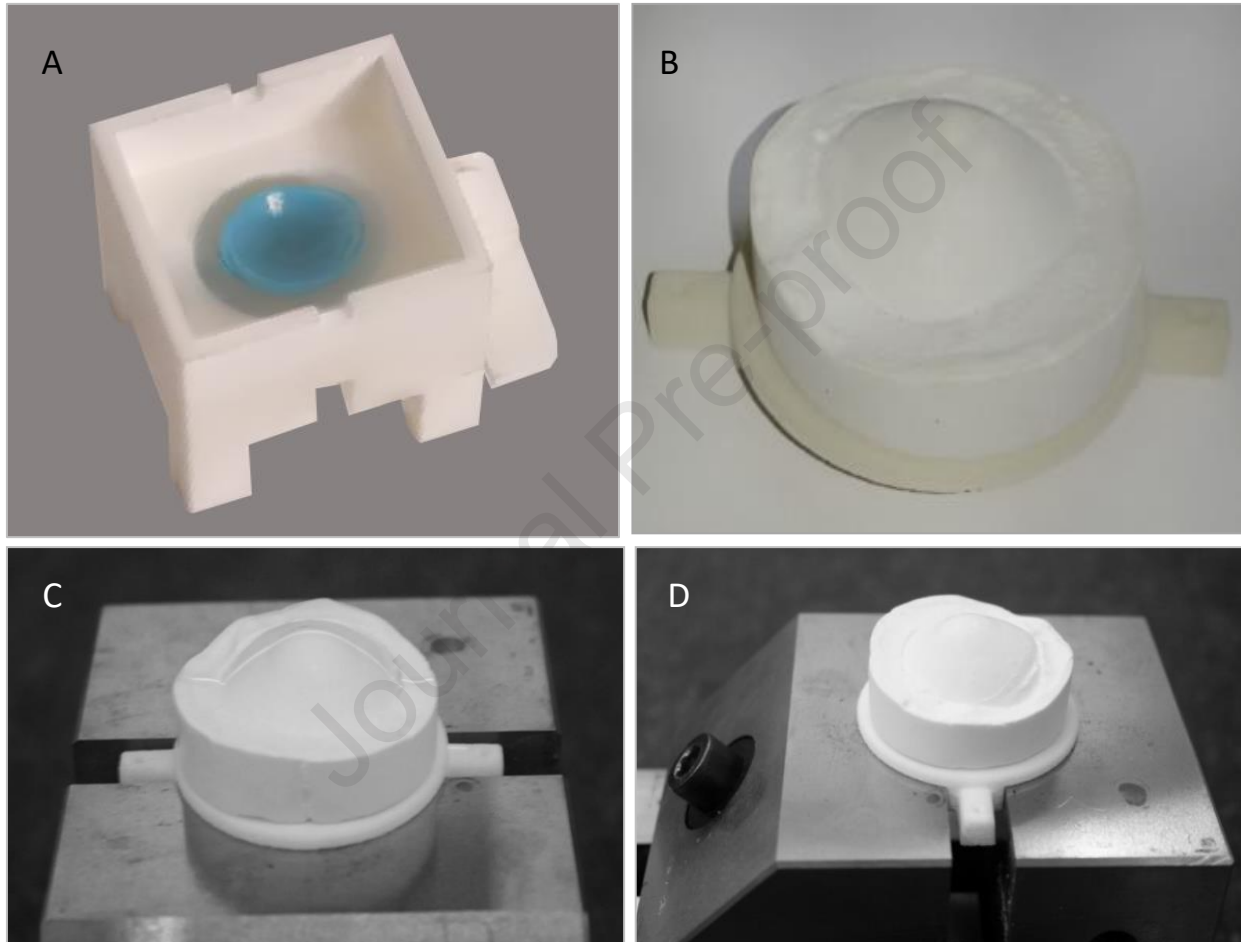
129 registration element (LRE) was designed, as shown in Figure 2 (A). In Figure 1, the LRE can be assembled to the  
 130 main frame of a device with the relevant direction and alignment based on the triangle landmarks. The LRE is  
 131 then used as the base of the AOS plaster cast or biomodel of the eye shape as shown in Figure 3 (B, C, D). This  
 132 method means that the LRE became an integral part of the AOS plaster cast once the plaster had set and adhered  
 133 to the polyamide material of the LRE. The LRE is aligned with the vertical meridian of the impression casting tray  
 134 and was held in position during the cast drying period by two notches in the casting support device (Figure 1).



158 Figure 2: Design of a landmark registration element (LRE) showing alignment with the cardinal directions of the  
 159 eye (x, y, z). A: The LRE with the introduced triangle marks to show the vertically aligned ridge on the LRE inferior  
 160 surface. B: The coordinate systems XYZ for the eye are used for registration and processing of the scanned data  
 161 points. C: The AOS profiles created from the scanned point cloud data of the AOS plaster cast or biomodel of the  
 162 eye shape. D: The AOS cross-profile in the XZ plane. The red curve is the AOS cross-profile in the XZ plane, and the  
 163 curvature at different positions of the AOS cross-profile is shown in green.

165 In this way, the datum of the ocular impression casting tray is “systematically” determined; and is consistent  
 166 from the eye impression process to the scanned 3D data set (Figure 2). This is important because the less

167 involvement of manual methods and the more consistence in the way in which the data is collected, the better  
168 the solution in the further analysis steps that will be obtained. It is noted that, the base of the LRE was designed  
169 to include a ridge that could be clamped into the fixture or jig for the Reverse Engineering (RE) process, in which  
170 high-precision laser scanners and co-ordinate measurement machines (CMMs) can be used to collect point cloud  
171 data that represent the geometry of the AOS shape. The casting support device and the LRE were manufactured  
172 using Additive Manufacturing (AM) or 3D Printing, the selective laser sintering (SLS) process (Figure 3).



192 Figure 3: A: The 3D printed casting support device with an impression casting tray in place in which the locking  
193 device is on the upper right side. B: The AOS plaster cast or biomodel of the AOS shape, in which the LRE is an  
194 integral part of the AOS plaster cast once the plaster had set and adhered to the polyamide material of the LRE.  
195 C & D: The base of the LRE was designed to include a ridge that could be clamped into the fixture or jig for the RE  
196 process, in which high-precision laser scanners and CMMs can be used to collect point cloud data that represent  
197 the geometry of the AOS shape.

199 An ocular impression casting tray was scanned using a touch-trigger probe installed on a Mitutoyo CMM machine  
200 - CRA Apex C Model (2005) (Mitutoyo (UK) Ltd, Andover, UK). The digitised surface data of the impression tray  
201 was then exported to the RE software package (Geomagic, 3D Systems Inc, South Carolina, USA) and a non-

202 uniform rational B-spline (NURBS) CAD model of the AOS shape was reconstructed, with the 3D cross profiles  
203 shown in Figure 2 (C, D).

204

205 The produced 3D printed casting support device with an impression casting tray in place is presented in Figure  
206 3 (A), in which the locking device is on the upper right side, and the AOS plaster cast or biomodel of the AOS  
207 shape which were successfully fabricated with the Type IV dental stone material (ULTIMA Novadur™), using the  
208 casting support device and the LRE in shown in Figure 3 (B). As mentioned, the base of the LRE included a ridge  
209 that could be clamped into the fixture or jig for the RE process (Figure 3 (C, D)), in which high-precision laser  
210 scanners and CMMs were used to collect point cloud data that represents the geometry of the AOS shape. Both  
211 non-contact and contact techniques of RE were used for data collection to reconstruct 3D models of the AOS shape  
212 from the AOS plaster casts.

213

#### 214 ***Prototyping and testing of a surrogate AOS biomodel***

215 The accuracy of reproducibility and the stability of the AOS biomodels are important for reconstruction of 3D CAD  
216 models of the AOS shape. In addition, the selection of relevant data collection methods, including the contact  
217 method using the CMMs with the touch-trigger probes and the non-contact method using the high-precision  
218 laser scanners, depends very much on the property of a material used for fabricating AOS biomodels. The  
219 shrinkage issues also need to be taken into account. Therefore, it is necessary to investigate the repeatability  
220 and reproducibility of the data collection methods, and to develop an optimal solution for data collection and  
221 processing to minimise possible errors and inconsistency when working on the point data processing to  
222 reconstruct 3D CAD models of the AOS shape. A single stainless-steel ball with a diameter of 22mm was cast as  
223 a surrogate AOS biomodel using the polyvinylsiloxane impression material Tresident™ (Shütz Dental Group  
224 GmbH, Germany), which was used for (1) evaluations of material selection and stability of the AOS biomodels  
225 which are fabricated using the casting support device and LRE, and (2) evaluation of repeatability and  
226 reproducibility of the data collection methods, using the contact and non-contact methods (CMMs and high-  
227 precision laser scanners). A previous study by our group found that Tresident™ was quicker, more effective, and  
228 produced less ocular surface staining than an alternative irreversible hydrocolloid material [5]. Tresident™ also  
229 has minimal impression shrinkage (0.2%–1% shrinkage after 24 hrs.) and is unaffected by humidity [5].

230

231 Tresident™ was dispensed into an impression shell and the shell/material combination pressed against the  
232 stainless-steel ball. Extra-hard, white plaster, Novadur™ (Ultima, Seiches-sur-Loir, France), a Type 4 Gypsum  
233 plaster, which conforms to ISO 6873:2013 (International Organisation for Standards) [14], was identified as a  
234 suitable compound to be used in conjunction with Tresident™. This product has excellent adhesion to the  
235 polyamide powder used in the SLS manufacturing process which is used to fabricate the LRE. Importantly, the

236 published expansion of Novadur™ is only 0.15% after 2 hrs [5]. A series of 12 AOS biomodels (such as those  
237 shown in Figure 3 (B, C, D)) was manufactured using the same methods of fabricating a surrogate AOS biomodel  
238 of the 22 mm stainless-steel ball, using the casting support device and LRE (Figure 1).

239

240 The surrogate AOS biomodel of the 22 mm stainless-steel ball was scanned using a touch-trigger probe installed  
241 on a CMM Mitutoyo CMM machine - CRA Apex C Model (2005) (Mitutoyo (UK) Ltd, Andover, UK) to ensure a  
242 high accuracy of data collection and measurements ( $\pm 0.001$  mm) [15].

243

#### 244 ***Data acquisition and analysis of repeatability, reproducibility and stability of the AOS biomodels***

245 Non-contact methods, such as laser scanning, were not used in the repeatability and reproducibility (R&R) study and  
246 the investigation of stability of the AOS biomodels due to: (1) their low accuracy ( $\pm 20$ -25 microns) in comparison  
247 with a contact method using a touch-trigger or contact probe (1-5 microns); (2) the complexity in data processing of  
248 non-contact methods; and (3) the data collection and processing of the contact method using Renishaw touch-  
249 trigger probes (Renishaw plc, Wotton-under-Edge, UK) installed in the CMM can be implemented automatically  
250 through CMM programs and data processing algorithms.

251

252 Figure 4 presents the data collection plan with the coordinate system or datum set-up for data collection using  
253 the CMM with the touch-trigger probes. The points of circular profiles are measured at different Z value:  $z = -1$   
254 mm,  $z = -2$  mm,  $z = -3$  mm,  $z = -4$  mm and  $z = -5$  mm. The CMM can be programmed to automatically measure  
255 the coordinates of points with respect to the established datum or part coordinate system. The distance  
256 between two points in each circular profile is about 0.5 mm. The Renishaw touch-trigger probe was used for  
257 data collection. The trigger force of touch probes can be adjusted, and the smallest trigger force was used to  
258 minimise the influence of contact forces on measurements. For Renishaw's touch-trigger probes, the trigger  
259 force range varies from 0.07 N to 0.5 N, depending on the stylus length and probe type [16].

260

261 With this data collection plan, to assess repeatability and reproducibility (R&R study) of the data collection method, 3  
262 surrogate AOS biomodels of the 22 mm diameter stainless-steel ball were used. There were, in total, 12  
263 measurements (4 measurements for each surrogate AOS biomodel of the stainless-steel ball) completed at  
264 different times and by different machine operators, using the same measurement program to operate the CMM  
265 (Mitutoyo CMM machine - CRA Apex C Model (2005), (Mitutoyo (UK) Ltd, Andover, UK). Each machine operator  
266 operated the CMM 4 times to measure the points that present the circular profiles. For each measurement, the  
267 points that present the circular profiles at different Z values ( $z = -1$  mm,  $z = -2$  mm,  $z = -3$  mm,  $z = -4$  mm and  $z$   
268  $= -5$  mm) were measured and the coordinates of these points were automatically generated in \*.asc file format.  
269 For better data management, the point data files and the AOS biomodels were coded as follow: (1) **Bb221**,

270 **Bb222** and **Bb223** indicates which surrogate AOS biomodel of the 22 mm diameter stainless-steel ball number  
 271 1, 2 and 3 respectively; and (2) the point data files **Bb221\_M1.asc** and **Bb221\_M2.asc** are created from the  
 272 measurements M1 and M2, respectively, for the surrogate AOS biomodel of the 22 mm diameter stainless-steel  
 273 ball number 1. The relevant codes are used for the point data files to assist in data acquisition and processing,  
 274 especially when using programming solutions to automate the steps of processing point data.

275

276

277

278

279

280

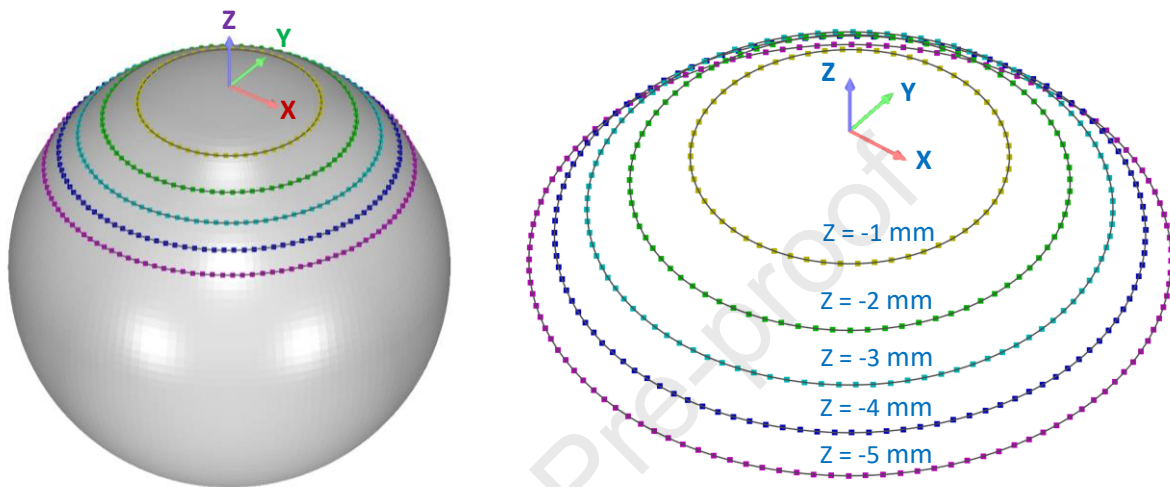
281

282

283

284

285



286 Figure 4: The datum set-up and the plan for data collection using the CMM with the touch-trigger probes, in  
 287 which the points of circular profiles are measured at different Z values:  $z = -1$  mm,  $z = -2$  mm,  $z = -3$  mm,  $z = -4$   
 288 mm and  $z = -5$  mm.  
 289

290 A laser scanning system, HYSKAN 45c (Hymarc Ltd, Ottawa, Canada), was also used for non-contact data  
 291 acquisition from the AOS biomodels of the 22 mm diameter stainless-steel ball, as well as the AOS biomodels of  
 292 the eye shape as shown in Figure 3 (B, C, D). With the use of laser scanning, there is no physical contact with the  
 293 AOS biomodels, and the data collection is very fast. The calibration accuracy of the laser scanning system is from  
 294  $\pm 0.020$  mm to  $\pm 0.025$  mm. While the laser scanning is known to be less accurate than point-to-point sensing with  
 295 touch-trigger probes, early testing using the model prototypes suggested that the combined system error of  
 296 the laser scanning and data processing was  $\pm 0.065$  mm (maximum), which is comparable to the repeatability  
 297 of modern ocular surface imaging methods and is close to the manufacturing tolerance for gas permeable  
 298 corneal contact lenses ( $\pm 0.05$  mm, back optic zone radius, (ISO 18369-2:2017; International Organisation for  
 299 Standards) and scleral contact lenses ( $\pm 0.1$  mm, back optic zone radius (ISO 18369-2:2017; (International  
 300 Organisation for Standards) [17].

301

302

303

304

305

306

307

308

309

310

311

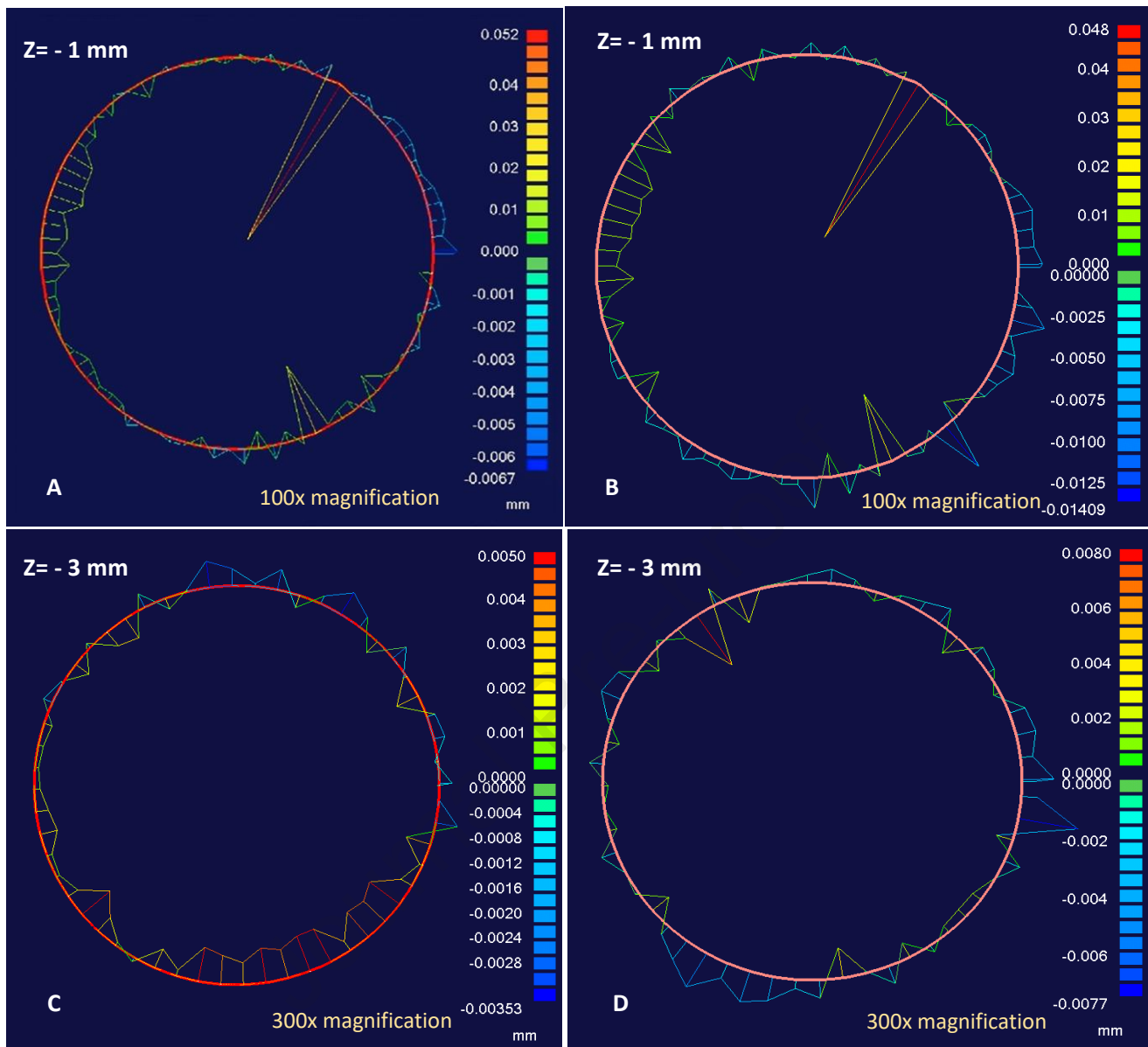
312

313

314

315

316



317

318

319

320

321

322

323

324

325

326

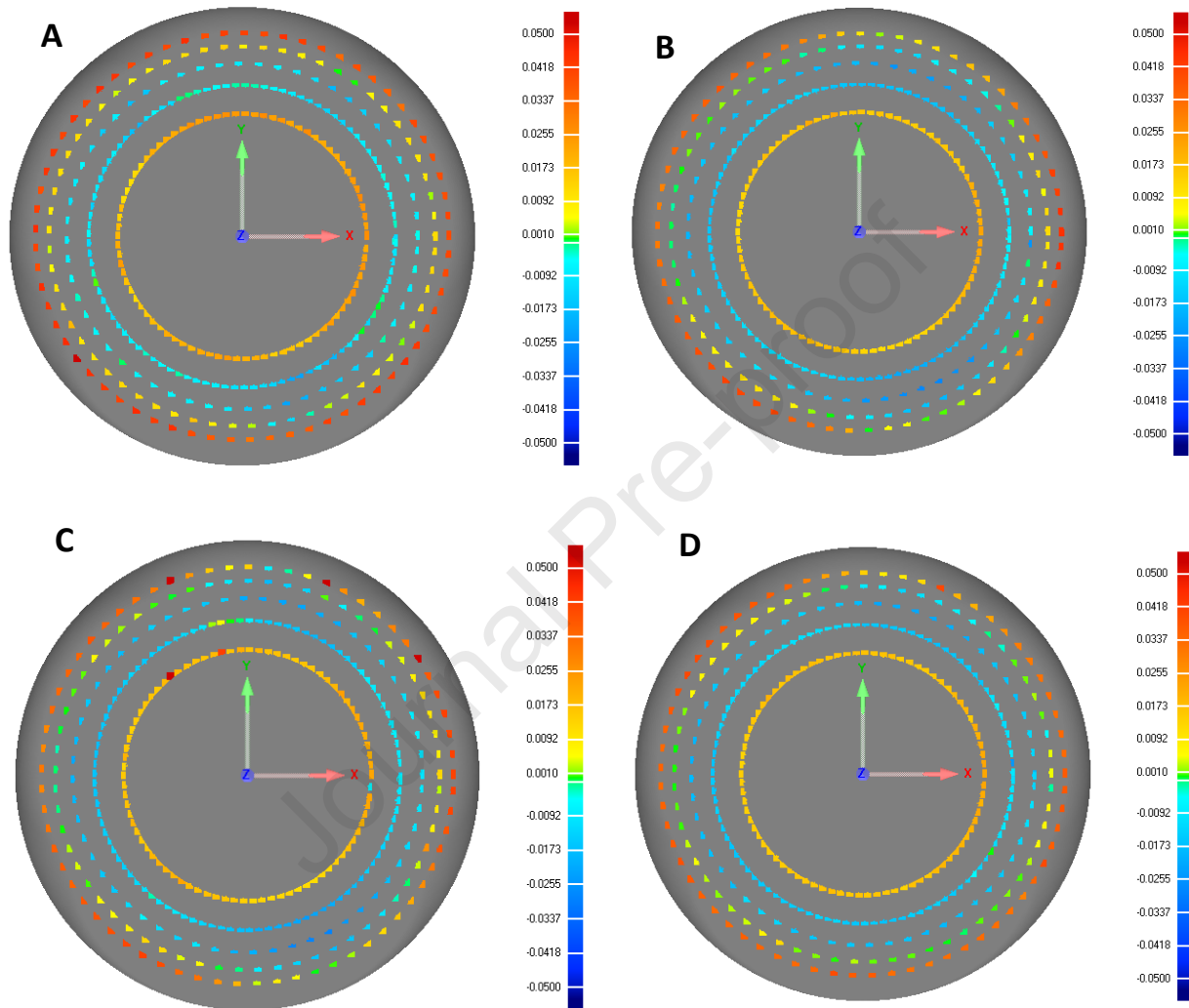
327

328 Figure 5: Example of the LSC radial plots showing comparisons of the measured 2D circular profiles of the surrogate  
 329 AOS biomodel **Bb221**. **A**: A comparison between the first and the second measurement in which a 2D circular  
 330 profiles were measured at  $z = -1$  mm. **B**: A comparison between the first and the third measurement in which a 2D  
 331 circular profiles were measured at  $z = -1$  mm. **C**: A comparison between the first and the second measurement in  
 332 which a 2D circular profiles were measured at  $z = -3$  mm. **D**: A comparison between the first and the third  
 333 measurement in which a 2D circular profiles were measured at  $z = -3$  mm. It is noted that, due to the size limitation  
 334 of the figure, the error map cannot be seen because of the small value of dimensional errors. A magnification of  
 335 100x and 300x was used to highlight the error maps in millimetres.  
 336

### 337 3. RESULTS

338 Measurements for each circle of sagittal depth were presented as radial plots or deviation maps using the least  
 339 squares circles (LSC) method [18]. This method produced a circle that shows the difference in the sum of the  
 340 squares of the deviation for the expected circle and the measurement data. Figure 5 presents an example of the

341 LSC radial plot showing a comparison between the first and second measurements of the surrogate AOS biomodel  
 342 **Bb221** (the 22 mm diameter stainless-steel ball number 1), measured at  $z = -1$  mm and  $z = -3$  mm, in which the  
 343 plots were colour-coded to provide a visualisation of positive error as hot colours (light green to red) and negative  
 344 error as cold colours (dark green to dark blue).



366 Figure 6: The deviation or error maps between the digitised points of the AOS biomodel **Bb221** of the 22 mm  
 367 diameter stainless-steel ball and the best fit sphere of all the digitalised points from 4 measurements. **A**: The  
 368 error map for the first measurement (**Bb221\_M1**). **B**: The error map for the second measurement (**Bb221\_M2**).  
 369 **C**: The error map for the third measurement (**Bb221\_M3**). **D**: The error map for the fourth measurement  
 370 (**Bb221\_M4**).  
 371

372 For a better understanding and investigation of repeatability, reproducibility and stability of the AOS  
 373 biomodels, the deviation or error maps between the digitised points of the AOS biomodel of the 22 mm  
 374 diameter stainless-steel ball and the best fit sphere of all the digitalised points from 4 measurements were  
 375 created (Figure 6).

376

377 Table 1 presents the summary about the deviation or error maps shown in Figure 6, for the 4 measurements  
 378 of the AOS biomodel **Bb221** of the 22 mm diameter stainless-steel ball, respectively **Bb221\_M1**, **Bb221\_M2**,  
 379 **Bb221\_M3** and **Bb221\_M4**.

380

381 Table 1: The deviation analysis between the digitised points of the AOS biomodel **Bb221** of the 22 mm diameter  
 382 stainless-steel ball and the best fit sphere of all the digitalised points from 4 measurements. RMS stands for  
 383 Root Mean Square.  
 384

	<b>Bb221_M1</b>	<b>Bb221_M2</b>	<b>Bb221_M3</b>	<b>Bb221_M4</b>
Positive Maximum Distance	0.0501	0.0456	0.1048	0.0406
Negative Maximum Distance	-0.0233	-0.0279	-0.0288	-0.0249
Average Distance	0.0096	0.0022	0.0031	0.0038
Positive	0.0237	0.0187	0.0199	0.0190
Negative	-0.0090	-0.0138	-0.0135	-0.0137
Standard Deviation	0.0194	0.0186	0.0197	0.0187
RMS Estimate	0.0216	0.0187	0.0200	0.0191

385

386 Similarly, the error maps for comparison of the digitised points of the AOS biomodels **Bb221**, **Bb222** and **Bb223**  
 387 and the best fit sphere of all the digitalised points from 12 measurements were created (Appendix 1), and the  
 388 summary about the deviation or error maps is presented in Table 2. The data from Tables 1 and 2 show that,  
 389 the repeatability and reproducibility of the data collection methods are acceptable.

390

391 The shrinkage study of the AOS biomodels was conducted with measurements taken one month apart for  
 392 comparison. The analysis results showed that most of the surrogate AOS biomodels reduced in size but within  
 393 an acceptable tolerance, in which the mean error is from 0.005 to 0.010 mm for the 2D circular profiles  
 394 measured at  $Z = -4$  mm.

395

396

397

398

399

400

401

402

403

404 Table 2: The deviation analysis between the digitised points of the AOS biomodels **Bb221**, **Bb222** and **Bb223** of  
 405 the 22 mm diameter stainless-steel ball and the best fit sphere of all the digitalised points from 12  
 406 measurements. RMS stands for Root Mean Square.  
 407

	<b>Bb221_1b</b>	<b>Bb221_2b</b>	<b>Bb221_3b</b>	<b>Bb221_4b</b>	<b>Bb222_1b</b>	<b>Bb222_2b</b>
Positive Maximum Distance	0.0274	0.0237	0.0791	0.0190	0.0522	0.0492
Negative Maximum Distance	-0.0338	-0.0410	-0.0405	-0.0371	-0.0813	-0.0521
Average Distance	-0.0034	-0.017	-0.0099	-0.0092	-0.0083	-0.0017
Positive	0.0167	-0.0170	0.0134	0.0123	0.0167	0.0195
Negative	-0.0174	0.0121	-0.0227	-0.0224	-0.0242	-0.0155
Standard Deviation	0.0177	0.0181	0.0191	0.0177	0.0250	0.0194
RMS Estimate	0.0180	0.0210	0.0215	0.0200	0.0264	0.0195

408

	<b>Bb222_3b</b>	<b>Bb222_4b</b>	<b>Bb223_1b</b>	<b>Bb223_2b</b>	<b>Bb223_3b</b>	<b>Bb223_4b</b>
Positive Maximum Distance	0.0412	0.0461	0.1035	0.01150	0.01465	0.01154
Negative Maximum Distance	-0.0414	-0.0410	-0.1144	-0.1068	-0.0063	-0.01043
Average Distance	-0.0015	-0.0020	0.0236	0.0292	0.0290	0.0320
Positive	0.0169	0.0176	0.0358	0.0377	0.0386	0.0392
Negative	-0.0144	-0.0154	-0.0173	-0.0192	-0.0184	-0.0220
Standard Deviation	0.0172	0.0177	0.0326	0.0320	0.0331	0.0317
RMS Estimate	0.0173	0.0178	0.0402	0.0433	0.0440	0.0451

409

#### 410 **4. DISCUSSION AND CONCLUSIONS**

411 This paper describes the investigation of a method of transferring the anatomical registration from an ocular  
 412 impression to a plaster cast representation, and reports on the validation of the method, which we have called  
 413 the Cardiff Eye Shape Analysis Protocol (CESAP). It provides evidence to support the use of the protocol for wide  
 414 field topographic data collection using ocular impression from the human AOS *in-vivo*, to a standard acceptable  
 415 to industry and clinical requirements.

416

417 Detailed knowledge of AOS topography is essential for ophthalmic clinical practice that involves eye shape.  
 418 Measurement based on optical methods has been the most common approach due to their speed of  
 419 measurement and analysis. However, optical methods are limited, with some exceptions [1, 7], to the corneal  
 420 region, due to a deterioration in the sharpness of the optical reflections in limbal area and across the  
 421 conjunctiva. The increasing use of scleral lenses for optical correction and ocular surface disease management  
 422 has increased the interest in AOS shape beyond the cornea [8, 9]. AOS impression-taking using a mouldable

423 material has been a longstanding method for large scale AOS representation and has been used in the  
424 manufacture of prosthetic eye shells and scleral contact lenses. However, detailed analysis of the change in  
425 AOS shape at the small scale, using laser scanning, has not been made until recently [4]. A significant challenge  
426 for accurate measurement has been a consistent method for producing the solid, 'real', plaster model of the  
427 AOS. Plaster casting, by itself is very simple, but a consistent approach for registration of the orientation of the  
428 AOS is more challenging. The results from this paper demonstrate that the Cardiff Eye Shape Analysis Protocol  
429 (CESAP) provides a repeatable and consistent method for producing solid, white plaster representations of the  
430 AOS biomodels.

431  
432 This investigation has provided evidence to validate the combined use of ocular impression taking and the  
433 CESAP to provide a reliable system for collecting topographic data for a surrogate AOS biomodels of the 22 mm  
434 diameter stainless-steel ball. The casting support device and landmark registration elements, when combined,  
435 can provide a consistent orientation registration system. Individual casts made from a series of impressions (using  
436 Tresident™ material and cast using Novodur™ plaster) were consistent in repeatability, reproducibility, and stability  
437 of material. The measurements were highly repeatable with an acceptable tolerance; for the case of **Bb221**, the  
438 average distance of the digitised points to the best fit sphere of all the digitalised points from 4 measurements is  
439 from 0.002 to 0.010 mm.

440  
441 This protocol for obtaining consistent 'real' AOS shape has several applications. Firstly, surface impression-  
442 taking, combined with plaster casting and reverse engineering, allows the comparison of a 'virtual' optical  
443 method with the 'real' surface shape. This permits the testing of instrument accuracy and provides a method  
444 for improving calibration.

445  
446 Secondly, by having an accurate digital representation of the ocular surface, the design and manufacture of  
447 prosthetic shells and custom scleral lenses can be improved [19]. Scleral lens manufacture using ocular  
448 impression-taking is long-established. CESAP provides a high level of accuracy which is important in the  
449 manufacture of custom designs for highly irregular AOS shapes.

450  
451 Thirdly, CESAP enables a consistent approach, including landmark registration, that is essential when gathering  
452 ocular impressions to incorporate into a 'real' AOS database. In another study not reported here, CESAP was  
453 successfully applied to create a database of 3D models of real AOS shapes. Figure 7 presents the height contour  
454 maps of the mean geometry of the AOS shape, calculated from 120 AOS biomodels of the right eyes of a European  
455 population. This database can be used to better understand normative population topographical variation  
456 associated with ethnicity or refractive error or can be used to describe the variation of support the design and

457 development of new types of contact lenses.

458

459

460

461

462

463

464

465

466

467

468

469

470

471

472

473

474

475

476

477

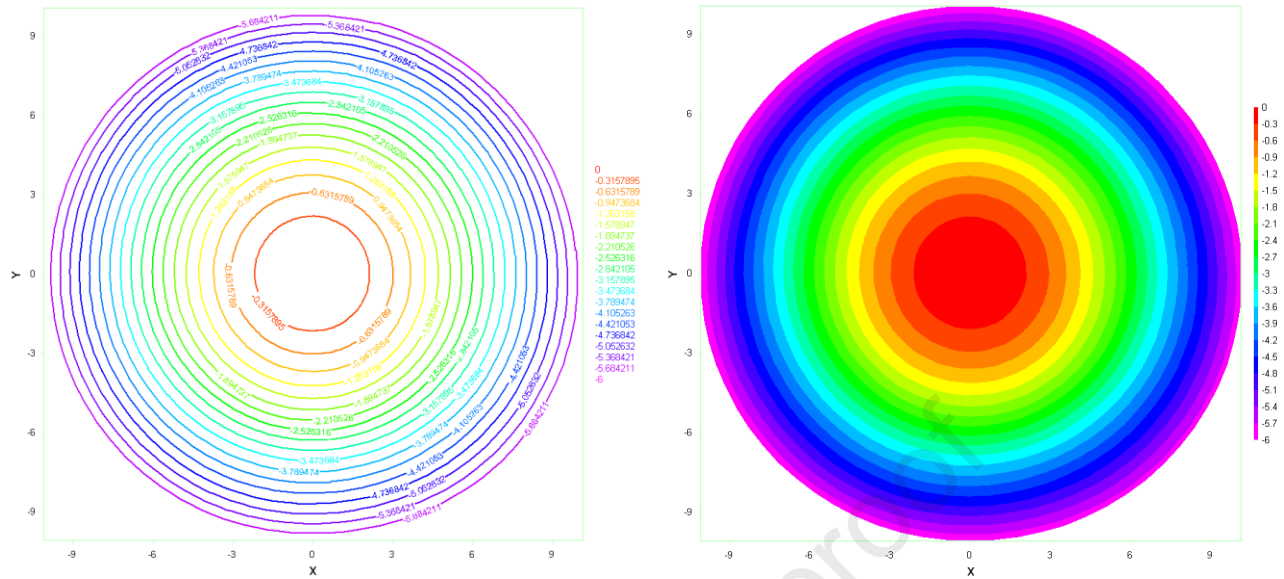
478

479

480

481

482



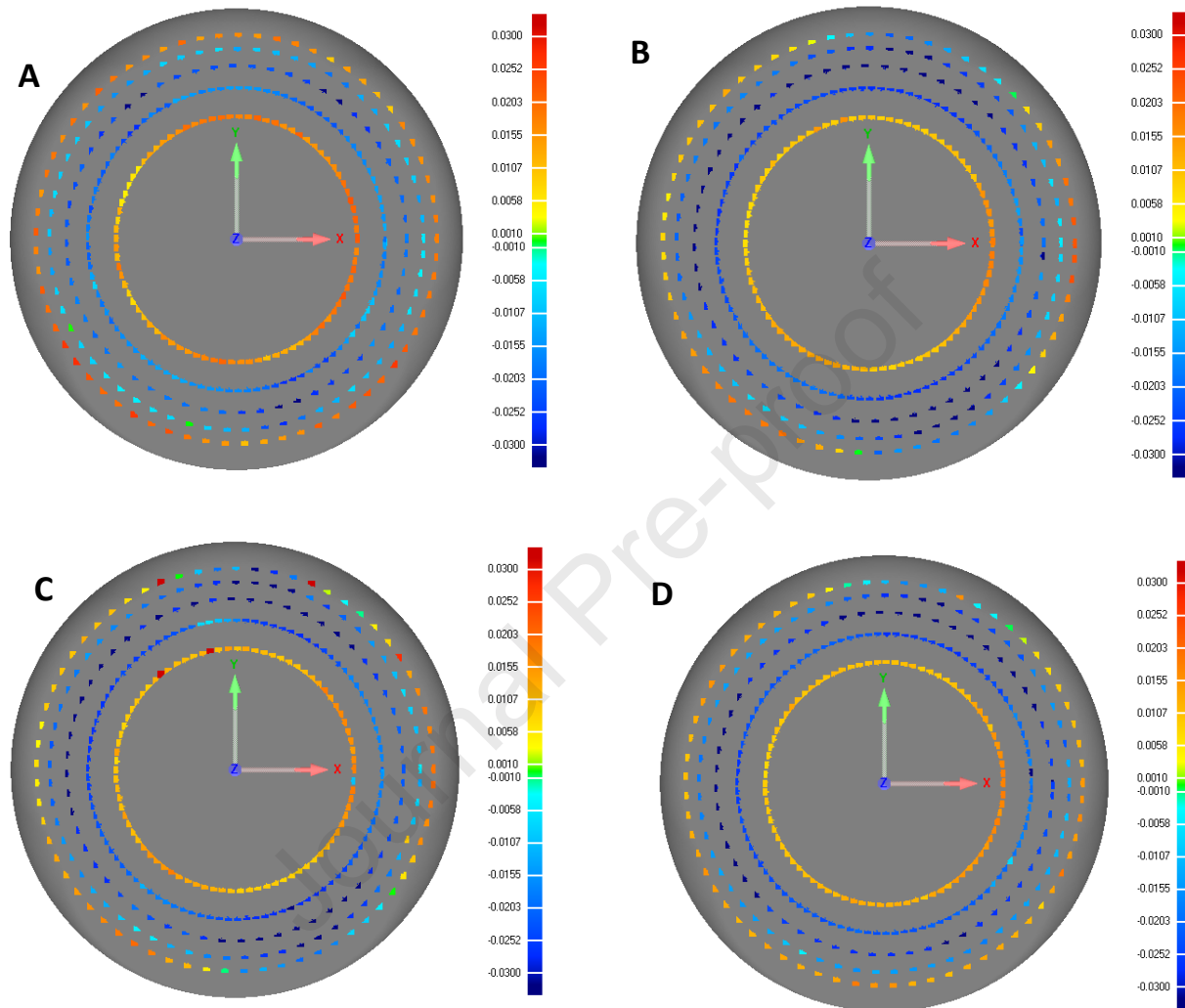
471 Figure 7: The height contour maps of the mean geometry of the AOS shape calculated from 120 AOS biomodels  
472 of the right eyes of the European population.

474 CESAP provides a framework for consistently converting an ocular impression into a 'real' AOS model that can  
475 be reverse engineered to create 3D CAD models of the AOS shape. These 3D CAD models have potential  
476 applications in optical image (topographer) calibration, prosthetic shell and scleral lens design, and AOS  
477 database development.

### 479 Funding

480 This study was supported by a collaborative partnership between Cardiff University and Menicon (Japan) Ltd.  
481 The authors have no proprietary or commercial interests in any of the materials discussed in this article.

483 **Appendix 1:** The deviation or error maps between the digitised points of the AOS biomodels **Bb221**, **Bb222**,  
 484 **Bb223** and **Bb224** of the 22 mm diameter stainless-steel ball and the best fit sphere of all the digitalised points  
 485 from 4 measurements.  
 486  
 487



498  
 499  
 500  
 501  
 502  
 503  
 504  
 505  
 506  
 507  
 508  
 509 Figure A1: The deviation or error maps between the digitised points of the AOS biomodel **Bb221** of the 22 mm  
 510 diameter stainless-steel ball and the best fit sphere of all the digitalised points from 4 measurements. **A:** The  
 511 error map for the first measurement (**Bb221\_M1**). **B:** The error map for the second measurement (**Bb221\_M2**).  
 512 **C:** The error map for the third measurement (**Bb221\_M3**). **D:** The error map for the fourth measurement  
 513 (**Bb221\_M4**).  
 514

515  
 516  
 517  
 518  
 519

520  
521  
522  
523  
524  
525  
526  
527  
528  
529  
530  
531  
532  
533  
534  
535  
536  
537  
538  
539  
540  
541  
542  
543  
544  
545  
546  
547  
548  
549  
550  
551  
552  
553  
554

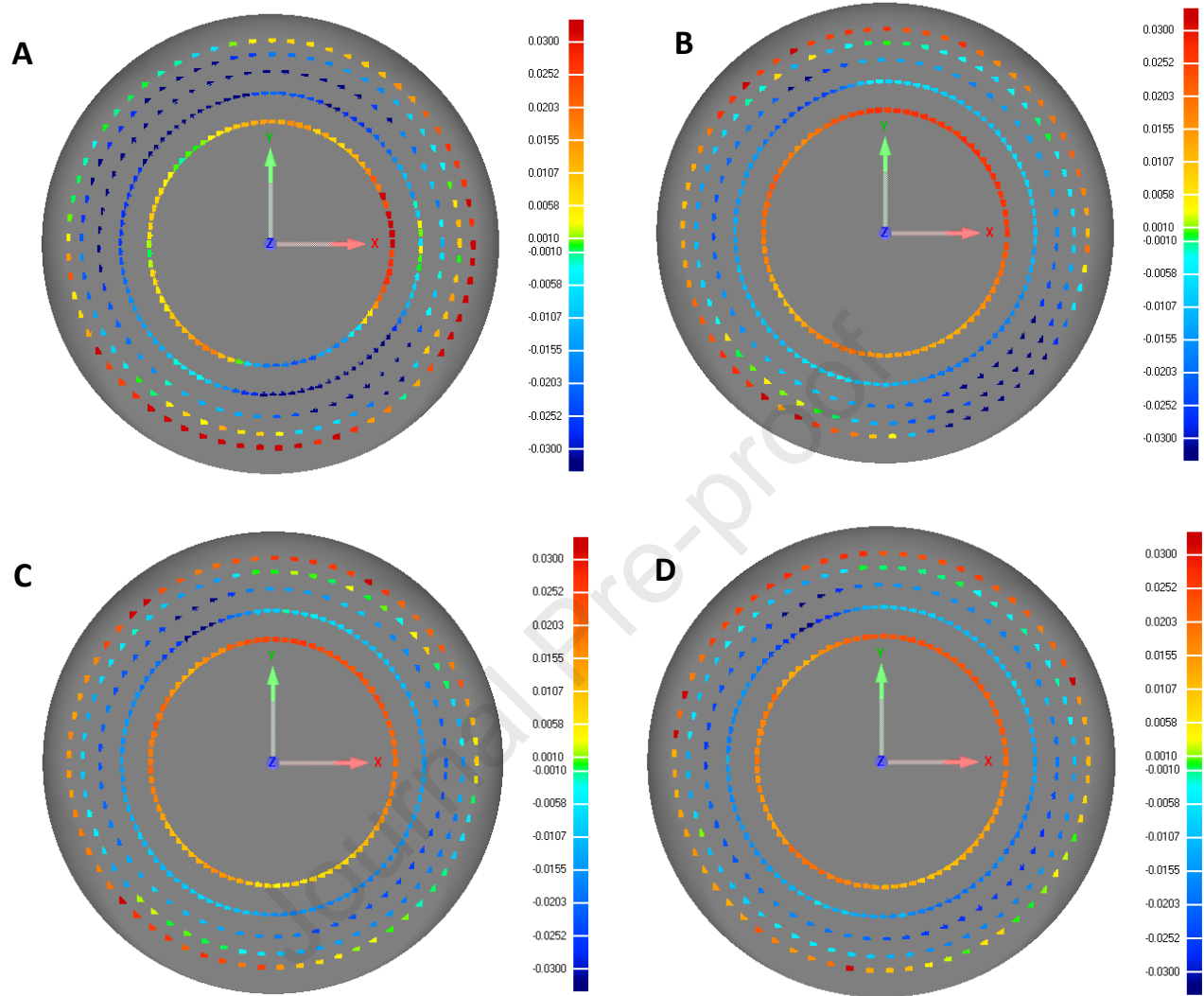


Figure A2: The deviation or error maps between the digitised points of the AOS biomodel **Bb222** of the 22 mm diameter stainless-steel ball and the best fit sphere of all the digitalised points from 4 measurements. **A**: The error map for the first measurement (**Bb222\_M1**). **B**: The error map for the second measurement (**Bb222\_M2**). **C**: The error map for the third measurement (**Bb222\_M3**). **D**: The error map for the fourth measurement (**Bb222\_M4**).

555

556

557

558

559

560

561

562

563

564

565

566

567

568

569

570

571

572

573

574

575

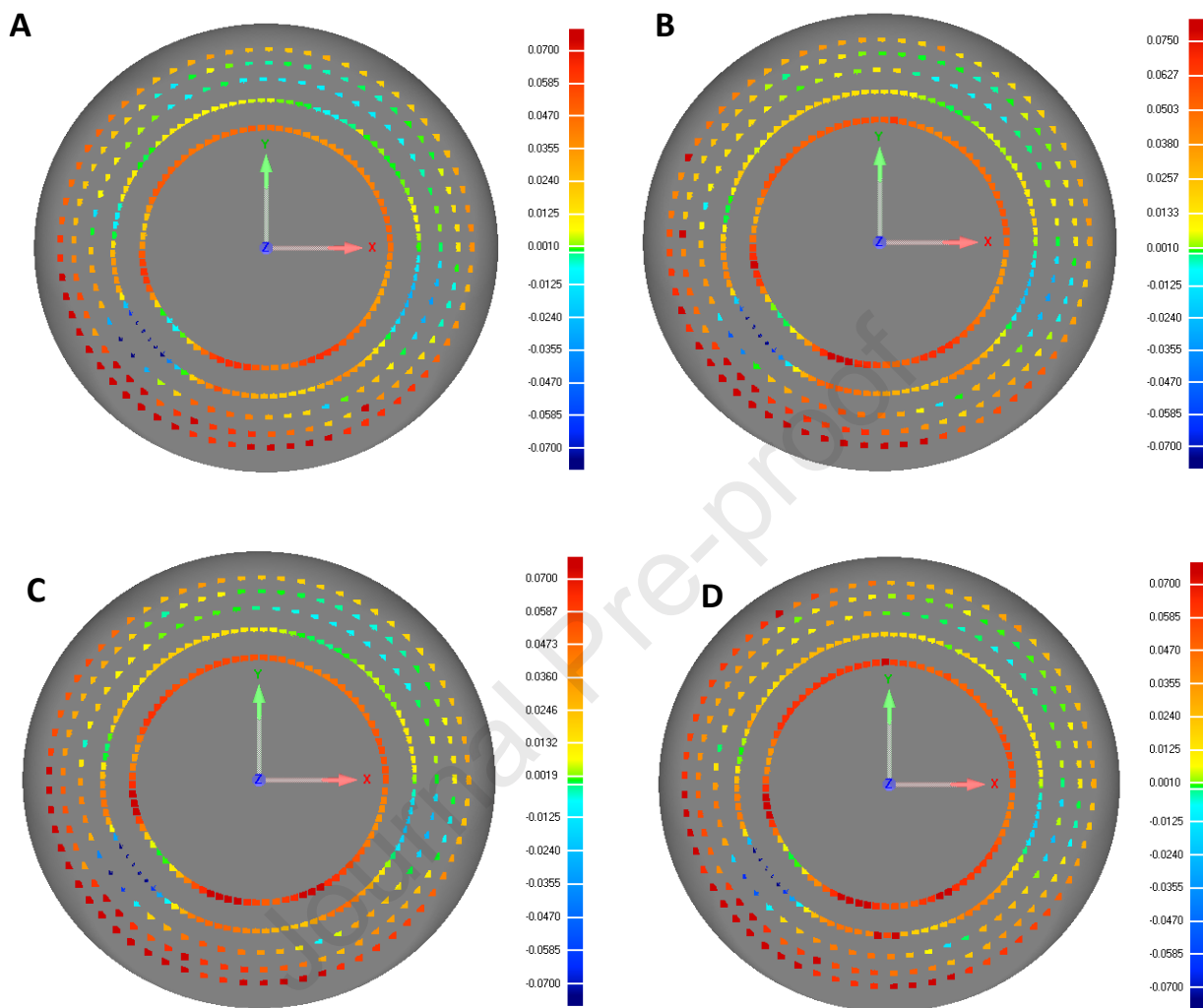
576

577

578

579 Figure A3: The deviation or error maps between the digitised points of the AOS biomodel **Bb223** of the 22 mm  
580 diameter stainless-steel ball and the best fit sphere of all the digitalised points from 4 measurements. **A**: The  
581 error map for the first measurement (**Bb223\_M1**). **B**: The error map for the second measurement (**Bb223\_M2**).  
582 **C**: The error map for the third measurement (**Bb223\_M3**). **D**: The error map for the fourth measurement  
583 (**Bb223\_M4**).  
584

585



586 **REFERENCES**

- 587 [1] Iskander DR, Wachel P, Simpson PN, Consejo A and Jesus DA (2016) Principles of operation, accuracy and  
588 precision of an Eye Surface Profiler. *Ophthalmol Physiol Opt* 36: 266–278.
- 589 [2] Pullum KW (2007). Eye Impressions. In: Phillips AJ, Speedwell L and Morris J [eds.] *Contact Lenses*. (5 ed.)  
590 Elsevier Butterworth-Heinemann, p. 343.
- 591 [3] Barnett M, Courey C, Faddi D, Lee K, Michaud L, Montani G, van der Worp E, Vincent SV, Walker M, Bilkhu P  
592 and Morgan P (2021). BCLA CLEAR – Scleral lenses. *Cont Lens Anterior Eye* 44: 270-288.
- 593 [4] Nau A, Shorter ES, Harthan JS, Fogt JS, Nau CB and Schornack M (2021). Multicentre review of impression-  
594 based scleral devices. *Cont Lens Anterior Eye* 44: 1-6
- 595 [5] Turner JM, Purslow C and Murphy PJ (2019). Ocular impression-taking – which material is best? *Eye Contact*  
596 *Lens* 45: 55-60.
- 597 [6] Bowden TJ (2009). Development of scleral contact lenses. In: *Contact Lenses, The Story*. Kent: Bower House  
598 Publications, pp. 76-86.
- 599 [6] Consejo A, Llorens-Quintana C, Radhakrishnan H and Iskander DR (2017). Mean shape of the human limbus.  
600 *J Cataract Refract Surg* 43:667-672.
- 601 [7] DeNaeyer G, Sanders D, van der Worp E, Jedlicka J, Michaud L and Morrison S (2017). Qualitative assessment  
602 of scleral shape patterns using a new wide field ocular surface topographer: The SSSG Study. *J Contact Lens Res*  
603 *Sci* 1: 12-22.
- 604 [8] Ritzmann M, Caroline PJ, Börret R and Korszen E (2018). An analysis of anterior corneal shape and its role in  
605 the design and fitting of scleral contact lenses. *Cont Lens Anterior Eye* 41: 205-213.
- 606 [9] Muzyka-Woźniak M, Oleszko A, Stróżecki Ł and Woźniak S (2022). The corneo-scleral junction assessed with  
607 optical coherence tomography. *PLoS ONE* 17: e0278884
- 608 [10] Tuan KA, McDonald E and Sindt CW (2022). Population ocular topography analysis using impression-based  
609 elevation data. *Invest Ophthalmol Vis Sci* 63: 536 – A0234
- 610 [11] Jesus DA, Kedzia R, Iskander DR. (2017) Precise measurement of scleral radius using anterior eye  
611 profilometry. *Cont Lens Anterior Eye*. 40: 47–52.

- 612 [12] Sclafani L, Slater D, Lay B and Sindt CW (2017). Topographic elevation data to design scleral lenses. Invest  
613 Ophthalmol Vis Sci 58:3550.
- 614 [13] Sindt CW, Lay B and Danno R (2018) Repeatability and validation of Scheimpflug scleral data. Invest  
615 Ophthalmol Vis Sci. 59: 1774.
- 616 [14] ISO 6873:2013 Dentistry. Gypsum Products (Reviewed 2024). Geneva: International Organisation for  
617 Standards
- 618 [15] Pham DT and Chi Hieu Le (2008). Reverse engineering - Hardware and Software. In: Raja V and Fernandes KJ  
619 [ed.] *Reverse Engineering - An industrial perspective*. London: Springer-Verlag, pp. 33-69.
- 620 [16] Renishaw (2024). Trigger force gauge. Available at: <https://www.renishaw.com> [Accessed: 29/1/2025].
- 621 [17] ISO 18369-2:2017 Ophthalmic Optics. Contact Lenses (Reviewed 2023). Tolerances. Geneva: International  
622 Organisation for Standards.
- 623 [18] Sui W and Zhang D (2012). Four methods for roundness evaluation. Physics Procedia 24: 2159-2164.
- 624 [19] Reinhard J, Urban P, Bell S, Carpenter D and Sagoo MS (2024). Automatic data-driven design and 3D printing  
625 of custom ocular prostheses. Nat Commun 15: 1360.
- 626

**Declaration of interests**

The authors declare that they have no known competing financial interests or personal relationships that could have appeared to influence the work reported in this paper.

The authors declare the following financial interests/personal relationships which may be considered as potential competing interests:

Jennifer Turner reports financial support was provided by Menicon Co Ltd. If there are other authors, they declare that they have no known competing financial interests or personal relationships that could have appeared to influence the work reported in this paper.